



## Article

# Flow Cytometry with Anti-Diffraction Light Sheet (ADLS) by Spatial Light Modulation

Yanyan Gong<sup>1,†</sup>, Ming Zeng<sup>1,†</sup>, Yueqiang Zhu<sup>1,†</sup>, Shangyu Li<sup>1</sup>, Wei Zhao<sup>1,\*</sup> , Ce Zhang<sup>1,\*</sup>, Tianyun Zhao<sup>2</sup>, Kaige Wang<sup>1</sup>, Jiangcun Yang<sup>3</sup> and Jintao Bai<sup>1</sup>

<sup>1</sup> State Key Laboratory of Photon-Technology in Western China Energy, International Collaborative Center on Photoelectric Technology and Nano Functional Materials, Institute of Photonics & Photon Technology, Northwest University, Xi'an 710127, China

<sup>2</sup> School of Automation, Northwestern Polytechnical University, Xi'an 710072, China

<sup>3</sup> Department of Transfusion Medicine, Shaanxi Provincial People's Hospital, Xi'an 710068, China

\* Correspondence: zwbayern@nwu.edu.cn (W.Z.); zhangce@nwu.edu.cn (C.Z.)

† These authors contributed equally to this work.

**Abstract:** Flow cytometry is a widespread and powerful technique whose resolution is determined by its capacity to accurately distinguish fluorescently positive populations from negative ones. However, most informative results are discarded while performing the measurements of conventional flow cytometry, e.g., the cell size, shape, morphology, and distribution or location of labeled exosomes within the unpurified biological samples. Herein, we propose a novel approach using an anti-diffraction light sheet with anisotropic feature to excite fluorescent tags. Constituted by an anti-diffraction Bessel-Gaussian beam array, the light sheet is 12  $\mu\text{m}$  wide, 12  $\mu\text{m}$  high, and has a thickness of  $\sim 0.8 \mu\text{m}$ . The intensity profile of the excited fluorescent signal can, therefore, reflect the size and allow samples in the range from 0 (100 nm) to 10  $\mu\text{m}$  (e.g., blood cells) to be transported via hydrodynamic focusing in a microfluidic chip. The sampling rate is 500 kHz, which provides a capability of high throughput without sacrificing the spatial resolution. Consequently, the proposed anti-diffraction light sheet flow cytometry (ADLSFC) can obtain more informative results than the conventional methodologies, and is able to provide multiple characteristics (e.g., the size and distribution of fluorescent signal) helping to distinguish the target samples from the complex backgrounds.

**Keywords:** light sheet; anti-diffraction; high resolution; size measurement



**Citation:** Gong, Y.; Zeng, M.; Zhu, Y.; Li, S.; Zhao, W.; Zhang, C.; Zhao, T.; Wang, K.; Yang, J.; Bai, J. Flow Cytometry with Anti-Diffraction Light Sheet (ADLS) by Spatial Light Modulation. *Micromachines* **2023**, *14*, 679. <https://doi.org/10.3390/mi14030679>

Academic Editors: Klaus Stefan Drese and Nam-Trung Nguyen

Received: 6 February 2023

Revised: 15 March 2023

Accepted: 17 March 2023

Published: 19 March 2023



**Copyright:** © 2023 by the authors. Licensee MDPI, Basel, Switzerland. This article is an open access article distributed under the terms and conditions of the Creative Commons Attribution (CC BY) license (<https://creativecommons.org/licenses/by/4.0/>).

## 1. Introduction

Flow cytometry (FC) is a powerful analytical technique that enables rapid analysis of cells and particles in solutions flowing past a single or multiple laser intercept points [1]. Due to its ability to count, characterize, and sort cells, it has been widely used in cell analysis and disease diagnosis [2–5].

In the last three decades, several research groups around the world have been involved in the study of microfluidic flow cytometry [6–12]. There are various types of flow cytometers that have been developed, including acoustic focusing cytometers, cell sorters, imaging cytometers, mass cytometers, and cytometers for bead array analysis [1]. Acoustic focusing cytometry uses ultrasound to help focus cells for laser interrogation [13]. The advantage is that it does not require a high speed or large volume of sheath flow. However, it suffers from low throughput and complex and large equipment. The cell sorter separates cells by generating droplets with high-frequency oscillation of the liquid sample stream [14]. The droplets are then given a positive or negative charge and passed through a metal deflector plate. Eventually, they are directed to specific collection containers depending on their charge. The cell sorter has high separation purity and flexibility, but it has no sample detail information.

In combination with fluorescence microscopy, imaging flow cytometry (IFC) [15] allows rapid analysis of the morphology and multi-parameter fluorescence of biological samples at the single-cell level, while a high spatial resolution of IFC can only be achieved by sacrificing the throughput, i.e., the number of analyzed biological samples per second. For example, the time span required for imaging one cell using a charged coupled device (CCD) can be as short as 1 ms, which means a maximum throughput of only 1000 cells per second [16]. Additionally, IFC requires a large storage space and has a high analyzing time.

Mass cytometry combines time-of-flight mass spectrometry and flow cytometry [17]. Cells are labeled with heavy metal ion-labeled antibodies (usually from the lanthanide family) instead of fluorescent antibodies, and detected using time-of-flight mass spectrometry. Since fluorescent labeling is not used, no light compensation is required. However, the sample cells are destroyed and cannot be analyzed downstream. Using the cytometer for bead array analysis is a technique that detects the fluorescent beads specifically bonding to the samples. By evaluating the intensity of fluorescence, the number of samples associated with the beads can be quantified [18].

Conventional flow cytometry is usually “bulky” and has a relatively low separation purity [1]. With the fast development of microfluidics and miniature techniques, portable, highly integrated, and easy-to-operate flow systems have been developed in the last ten years [13,19,20]. For example, Jiang et al. designed a miniaturized dual-wavelength fluorescence detection chip by coupling electrokinetically induced pressure-driven flow for fluorescent particle counting [21]. Kanwa et al. used polydimethylsiloxane (PDMS) to fabricate a microfluidic device shaped like a gourd to capture and quantitatively analyze stained exosomes [22]. Lee et al. proposed an acoustic nano filter system that separates microvesicles of specific sizes in a continuous and contactless manner [23]. These new cell (or particle) detection devices have enriched the family of flow cytometry devices.

Nevertheless, the performance of FC is the compromise of one of the key parameters in favor of the others, hence limiting its applications. Morphological features of the biological samples are often among the key parameters that help to distinguish one population from another [16]. For example, *E. coli* is a typical Gram-negative rod bacterium whose length ranges from one to tens of micrometers and reflects distinctive activities [24]. In the conventional FCs where elliptical and spherical focal spots are adopted, the differences in the size, shape, and orientation of cells when passing through intercept points cannot be detected, which makes it difficult to distinguish the active cells [25]. In contrast, focal spots with a large aspect ratio (e.g., the light sheet) generate distinctive intensity profiles when a non-spherical object passes (Figure 1). Miura et al. [26] implement a light sheet into a customized IFC, which aims to boost the fluorescence intensity of each image pixel by a factor of ~10. To the best of our knowledge, none of these researchers utilize focal spots with a high aspect ratio to improve the spatial resolution of FC.

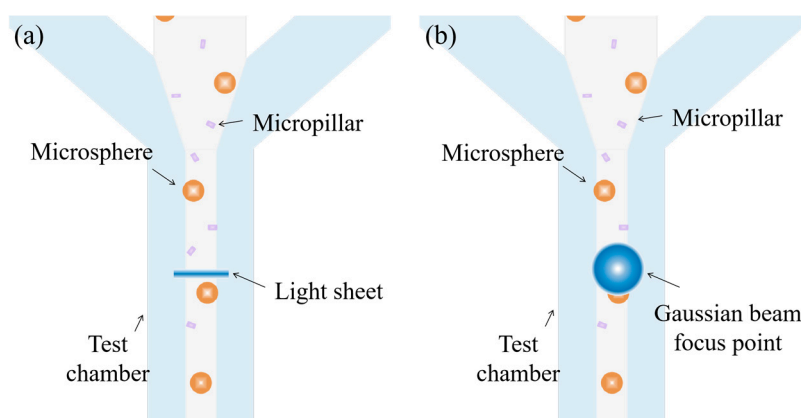


**Figure 1.** (a) Fluorescent micropillars and microspheres passing through a light sheet, and (b) fluorescent micropillars and microspheres passing through a Gaussian beam spot.

In this investigation, we designed a novel flow cytometry system using a highly anisotropic and anti-diffraction light sheet (ADLS) as the laser interception point. The ADLS was formed by a parallel and tightly aligned Bessel–Gaussian beam generated by a spatial light modulator (SLM) with the stripe split phase (SSP) method [27]. A Bessel–Gaussian beam is a type of beam with vectorial polarization. It has several amazing features, e.g., anti-diffraction, self-healing [28], large depth of focus, and low interference [29,30] even if two of them are parallel and tightly placed. Therefore, it is possible to generate ADLS using Bessel–Gaussian beam arrays with a large area and good uniformity. Additionally, the self-healing feature keeps the ADLS undistorted when passes through a complex solution [31]. In the current research, the dimensions of the ADLS are 12  $\mu\text{m}$  by 12  $\mu\text{m}$ , with 0.8  $\mu\text{m}$  thickness. This specification enables us to measure both large and small objects with submicron spatial resolution. Passing through objects with different sizes, distributions, and even attitudes (if the dimensions of the object are known) results in distinctive intensity profiles, which can be counted and analyzed. This is not achievable for the conventional FC. Coupled with a photomultiplier tube and high-speed data acquisition module, a 500 kHz sampling rate can be easily achieved. The maximum count rate can be at least  $10^4$  events per second. Therefore, the proposed methodology greatly improves the spatial resolution of conventional FC, and is suitable for sorting and analyzing biological samples with complex physical and chemical features.

## 2. System Setup

The experimental system is shown in Figure 2a. In this experiment, a 473 nm continuous wave (cw) laser (MW-RL-473, 200 mW, CNI, Changchun, China) is adopted as the light source. The laser beam is first filtered by a spatial light filter and then collimated by a beam expander. The beam is further adjusted through a beam splitter (THORLABS, BS 400~800 nm, Newton, NJ, USA) and a polarizer (P). After it passes through the polarizer, the direction of the linearly polarized beam is parallel to that of the liquid crystal (LC) of the SLM (PLUTO-NIR-011, 420~1100 nm, LETO, HOLOEYE Photonics AG, Berlin, Germany). The modulated beam is further guided into an inverted fluorescence microscope system (NIB900, NEXCOPE, Ningbo, China) and focused with an objective lens (Leica, L 20X, NA 0.4, Wetzlar, Germany) to generate an ADLS at the focus. The microscope has a set of filters, including a dichroic mirror (SEMROCK, IDEX Health & Science LLC, Di01-R488/543/635, 473 nm HR, Carlsbad, WA, USA) and a band-pass filter (CHROMA, ZET488/640 nm, Bellows Falls, VT, USA), to extract the fluorescence from the excitation light.

Particle detection, measurement, and analysis are achieved using the ADLS in a microfluidic chip fabricated for flow cytometry (inset of Figure 2a). The microchip has three inlets. The A and C inlets are for water flow, while the B inlet is for the sample solution. The three solutions come into contact at the joint O and form a sheath flow downstream. The microchannels AO, BO, and CO are 100  $\mu\text{m}$  in width and 10  $\mu\text{m}$  in height. The test chamber, i.e., the DO section, is 50  $\mu\text{m}$  in width and 10  $\mu\text{m}$  in height.

The spatial position of the microfluidic chip is changed by a nano-piezo stage (CB7 4EX, THORLABS, Newton, NJ, USA) so that the ADLS is located in the center of the microchannel. When the fluorescent particles pass through the ADLS at a given speed, the ADLS excites the fluorescent particles to emit fluorescence. The fluorescent signal passes through the band-pass filter and dichroic mirror in turn, then is captured by detectors. With a beam splitter in the microscope, 20% of the fluorescence is captured by a sCMOS camera (PCO edge 4.2LT, Kelheim, Germany, PCO) to monitor the ADLS. The remaining 80% fluorescence is focused into an optical fiber and detected with a photomultiplier tube (Hamamatsu Photonics, H7415, 300~650 nm, Hamamatsu, Japan) (PMT). The ADLS is placed in the test chamber to detect the samples in the jet flow, as shown in Figure 2c,d. In contrast, the zeroth order light spot is focused into the sheath flow. Only the fluorescence of samples passing through the ADLS can be focused into the optical fiber. The possible fluorescence excited by the zeroth order light has been blocked.

The PMT, combined with an amplifier (low gain  $\times 10^5$ , medium gain  $\times 10^6$ , and high gain  $\times 10^7$ ), converts fluorescence signals into electrical signals. Then, after being collected and converted into digital raw data by a 16-bit analogue-to-digital converter on an embedded board, the data are finally sent to a computer for processing and analysis. The sampling rate of the system is up to 500 kHz.

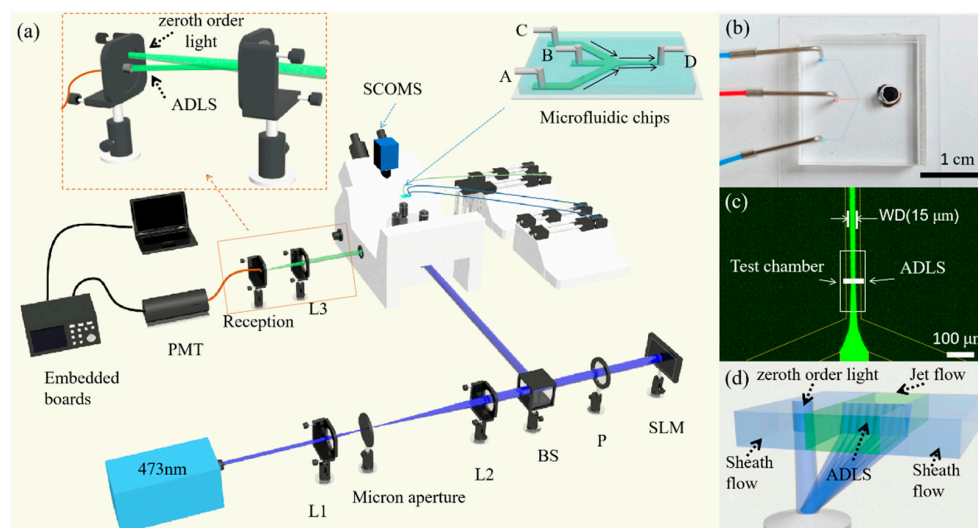


**Figure 2.** Schematic diagram of the ADLSFC system. (a) Schematic of the system. (b) Photo of the microfluidic chip. (c) Fluorescence image of the microchannel. The inlets A and C are injected with pure water, and B is injected with fluorescein sodium salt solution. All inlets have flow rates of  $1 \mu\text{L/h}$ . The width of the jet (WD) is  $15 \mu\text{m}$ . D is the outlet. (d) Schematic diagram of the ADLS in the test chamber after focusing by the objective lens. Zeroth order light spot is separated with the modulated ADLS. The latter covers the entire jet flow, while the former is located in the sheath flow.

### 2.1. Fabrication of the Microfluidic Chip

The microchannel is fabricated through soft lithography with polydimethylsiloxane (PDMS) [22,32] as according to the procedure shown in Figure 3. The channel layer is first fabricated using a negative photoresist SU-8 3025 on a silicon wafer. After 10 min prebaking, the photoresist-coated wafer is exposed to UV light using a contact mask aligner (MIDAS, MDA400LJ, Daejeon, Republic of Korea). After post-baking (10 min) and development, the template is obtained. The structure of the template is subsequently duplicated using PDMS. The PDMS microchannel is further bonded onto a glass slide and punched with inlets and outlets to form the desired microfluidic chip.

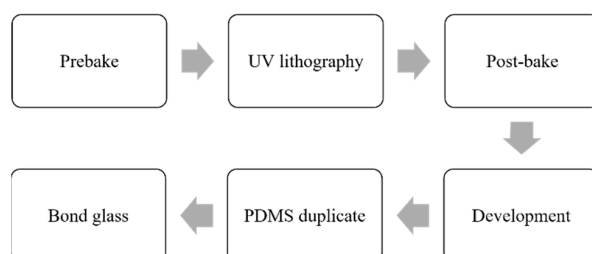


**Figure 3.** Fabrication process of the microfluidic chip.

### 2.2. Sample Preparation

To test the ADLSFC system, we used two kinds of fluorescent particles: polystyrene fluorescent micropillar ( $0.4\sim 1 \mu\text{m}$  long with  $0.3\sim 0.6 \mu\text{m}$  diameter) and  $5 \mu\text{m}$  diameter polystyrene fluorescent microspheres. Both of them have an excitation peak at  $468 \text{ nm}$  and an emission peak at  $508 \text{ nm}$  (Thermo Fisher Scientific, Waltham, MA, USA) (Figure 4a,b).

Both microparticles were diluted with ultrapure water. To prevent the fluorescent beads from sticking to the wall of the microchannel, surfactant of Pluronic F-127 (Merck, Pluronic F-127, Darmstadt, Germany) was added to the diluted solution, and the final concentration of Pluronic F-127 was less than 0.1%.

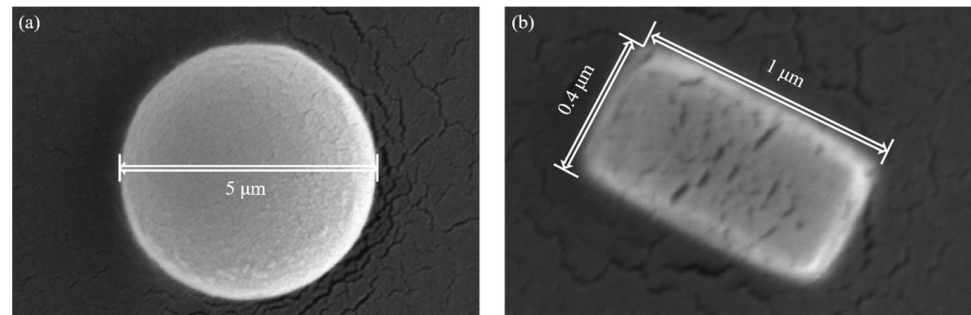


**Figure 4.** Scanning electron microscope (SEM) image of fluorescent particles. (a) Fluorescent microspheres. (b) A typical fluorescent micropillar.

In the experiment, we used two syringe pumps to provide the basic flow and deliver the microparticles. Three 50  $\mu\text{L}$  syringes are connected to the inlets A, B, and C of the microfluidic chip, with peek tubing and connectors. Water is injected into inlet A and C to provide sheath flow. Fluorescent microparticles are injected into inlet B. Before measurement, the microchannel was degassed in advance. The detection is carried out right after the sheath flow was formed stably. The particle velocities in the jet at different flow rates are obtained using a camera, as plotted in Figure 5. The ratio of each sheath flow rate ( $Q_s$ ) to the jet flow rate ( $Q_j$ ) is fixed at 1. For each flow rate, the particle velocity measurement is repeated 20 times. It can be seen the particle velocity increases with flow rate, accompanied with a higher velocity fluctuation. When  $Q_s$  or  $Q_j$  is less than 1  $\mu\text{L}/\text{h}$ , a stable sheath flow cannot be formed in the test chamber. Therefore, we choose 1  $\mu\text{L}/\text{h}$  as the experimental flow rate for both  $Q_s$  and  $Q_j$ . The average velocity ( $u_p$ ) of particles in the jet flow is 1.41 mm/s. The jet width (WD) in the test chamber is 15  $\mu\text{m}$ . The Reynolds number of flow in the test chamber is [33]

$$Re = \frac{\rho U_m D_h}{\mu} \quad (1)$$

where  $\rho$  is the fluid density,  $\mu$  is the dynamic viscosity of the fluid,  $U_m$  is the maximum velocity of the fluid, and  $D_h$  is the hydraulic diameter defined as  $D_h = 2hw_{ch}/(h + w_{ch})$ .  $w_{ch}$  is the width of the channel and  $h$  is the height of the channel. By substituting the values into Equation (1), we obtain the Reynolds number in the test chamber as  $2.78 \times 10^{-2}$ , indicating that the flow is laminar.

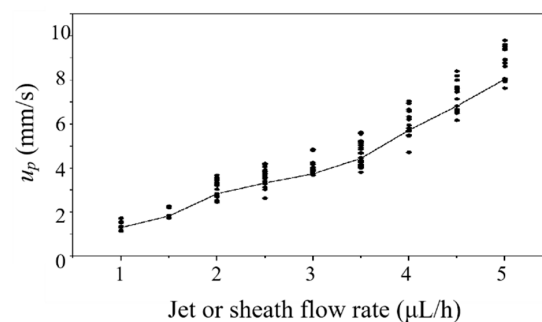


**Figure 5.** Fluorescent particle velocity varies with the jet or sheath flow rate. Here,  $Q_s:Q_j = 1:1$ . Each dot represents a measurement. The average velocity of the measurement is represented by the solid line.



### 2.3. Data Analysis

With a set flow rate, the speed of particle in the jet flow can be calculated as

$$u_p = kQ_{all}/hw_{ch} \quad (2)$$

where  $k$  is a correction coefficient and  $Q_{all} = Q_j + 2Q_s$  is the overall flow rate. Through experimentation, we obtained  $k = 0.83$  when the flow rates of jet and sheath flow are both  $1 \mu\text{L/h}$ . Then, the diameter ( $d_p$ ) of the particle can be estimated as

$$d_p = u_p \tau - d_s \quad (3)$$

where  $d_s$  is the thickness of the ADLS and  $\tau$  is the full width at half maximum (FWHM) of the pulse signal in time domain corresponding to the particle. In summary, after determining  $\tau$  of the particle, the particle size can be obtained directly relying on the particle speed.

The data processing algorithm includes five main steps, as diagrammed in Figure 6. (1) The raw data are first processed with a threshold filter and a bandpass filter to remove noise and pick the pulse regions from the raw data. (2) These pulse regions are smoothed with a moving average algorithm and the local maxima is searched for in the pulse regions. (3) The widths of the pulses from their rising and falling edges are determined, then the pulse data are validated with the bandpass filter again. (4) The validated pulse data are interpolated to calculate the  $\tau$ . (5) The process above is repeated, and the number and diameters of the particles are statistically calculate.

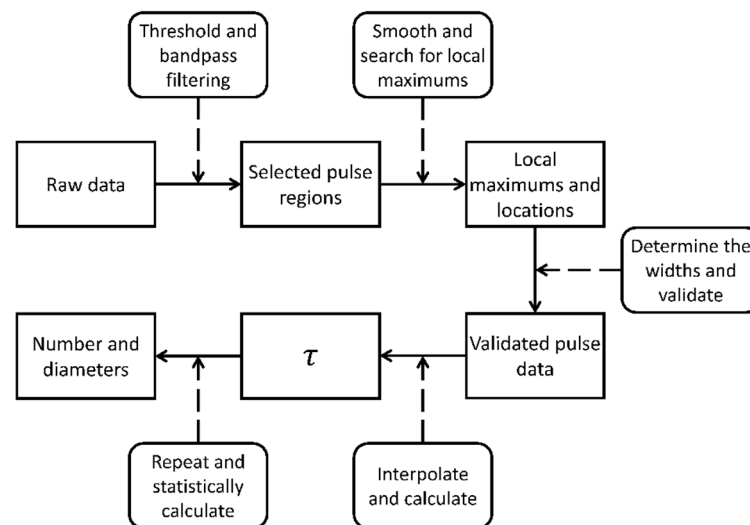


Figure 6. Diagram of data analysis.

### 3. Generation of ADLS

Conventional flow cytometers use a focused spot as the laser interrogation point. The axisymmetrically distributed focus spot cannot completely cover the microchannel interface, in the meanwhile obtaining the detailed information about the sample. In contrast, a highly anisotropic ADLS can cover the entire microchannel with a large area while reserving a small thickness to provide high resolution in the streamwise direction.

There are several ways of generating a light sheet, e.g., using a cylindrical lens, rapidly scanning the beam back and forth [34–36], and through coherent superposition of plane waves [37,38]. The formation of a light sheet through a cylindrical lens is easy to integrate into the optical path because it does not require moving parts, but the thickness of the light sheet is normally  $2\text{--}10 \mu\text{m}$  [39–42]. The fast-scanning beam method does not really generate a light sheet, and it is more suitable for detecting stationary samples. It could lose the samples in the detection of the flow system. The coherent superposition of plane waves can generate light sheets, but is sensitive to the aberration due to refraction indices mismatch.

Relative to the methods above, an SLM that can be easily integrated into the optical system to generate a thin light sheet as the laser intercept point is very suitable for developing novel flow cytometry. Through SLM, diverse laser spots with the desired properties, e.g., anti-diffraction beam, self-bending beam, and negative refractive index beams, etc., can be generated on demand. Due to the anti-diffraction feature of Bessel–Gaussian (BG) beam [43], numerous BG beams can be aligned sufficiently close to each other to form a light sheet (Figure 7a), i.e., ADLS, without significant influence of interference. A BG beam has a smaller diameter of focus than a Gaussian beam, but a much larger depth of focus. Therefore, the ADLS constituted of BG beams simultaneously reserves large areas with small thicknesses.

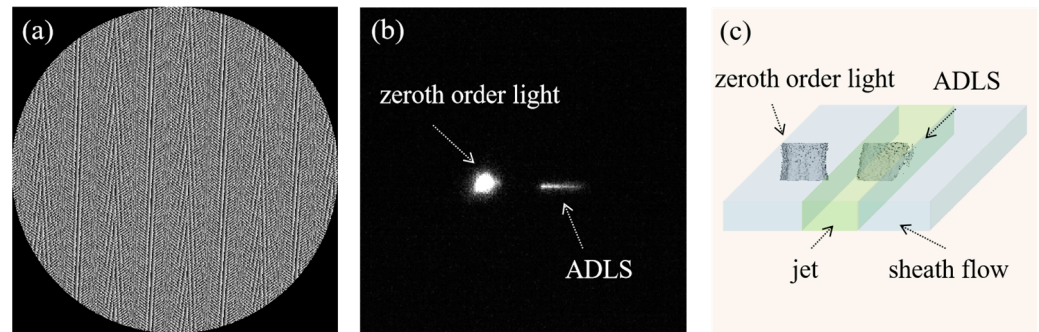


**Figure 7.** (a) The phase map of generating the ADLS. (b) Experimental visualization of the zeroth order light and ADLS with an inverted fluorescence microscope, using a 50  $\mu\text{mol/L}$  concentration fluorescein sodium salt (SIGMA, 46970-100G, Roedermark, Germany) solution. (c) 3D construction of the ADLS from fluorescent images using MATLAB software (MATLAB R2022a, Mathworks, Natick, MA, USA). The ADLS is 12  $\mu\text{m}$  wide, 12  $\mu\text{m}$  high, and 0.8  $\mu\text{m}$  thick.

The BG beam and the ADLS generated through SLM can be elucidated using Debye diffraction theory [43,44]. Based on the Fourier transform (FT) of the Debye diffraction integral and ignoring constant coefficients, the electric field intensity ( $E$ ) of light can be calculated by [27]

$$E(x, y, z) = \begin{bmatrix} E_x \\ E_y \\ E_z \end{bmatrix} = \begin{bmatrix} \int_0^\theta \int_0^{2\pi} \frac{p(\theta)E_t(\theta, \varphi)}{\cos \theta} e^{ik_z z} e^{i(k_x x + k_y y)} dk_x dk_y \\ F^{-1} \left[ p(\theta)E_t(\theta, \varphi) e^{ik_z z} / \cos \theta \right] \end{bmatrix} \quad (4)$$

where  $p(\theta)$  is the apodization function of the objective lens,  $E_t(\theta, \varphi)$  is the transmission electric field,  $\varphi$  is the azimuth angle of the objective lens,  $\theta = \arcsin(r_{\text{NA}}/Rn_t)$  is the convergence angle of the objective lens, and  $k_x, k_y, k_z$  are the wavenumbers in vacuum. Here,  $F^{-1}$  denotes inverse Fourier transform.

According to Equation (4), the electric field of the modulated beam is

$$E(x, y, z) = F^{-1} \left\{ \left[ e^{i\Phi} \right] P(\theta) E_t(\theta, \varphi) e^{ik_z z} / \cos \theta \right\} \quad (5)$$

where  $\Phi$  is the modulation phase function. In this investigation, to generate a Bessel–Gaussian beam with blazed grating simultaneously, we have

$$\Phi = \Phi_1 + \Phi_2 \quad (6)$$

where  $\Phi_1$  and  $\Phi_2$  are the phase functions for modulating blazed grating and Bessel–Gaussian beams. They can be expressed as [27]

$$\Phi_1(x', y') = \frac{2\pi}{\lambda} (x' \Delta x + y' \Delta y) \quad (7)$$

$$\Phi_2 = 2\pi r \tan \alpha / \lambda \quad (8)$$

where  $x', y'$  are the Cartesian coordinates in the pupil plane, NA is the numerical aperture of the objective lens,  $R$  is the maximum radius of the pupil plane of the objective lens, and  $n_t$  is the refractive index of the objective.  $r = \sqrt{x'^2 + y'^2}$  is the polar diameter in the plane of the pupil plane,  $\alpha$  is the apex angle of the angular pyramid prism, and  $\lambda$  is the wavelength. Finally, the light intensity after modulation can be calculated through  $I = |E|^2$ .

Given  $\Delta x, \Delta y$  for each Bessel–Gaussian beam, the ADLS formed by aligned Bessel–Gaussian beams can be generated. To achieve a uniform ADLS in the experiment, nine Bessel–Gaussian beams are generated and arranged in parallel at an interval of  $8\lambda$ . The BG array is generated via an SLM, with the phase map designed according to the strip segmentation phase (SSP) method [27], with a blazed grating superposed (Figure 7a). In order to calibrate the dimensions of the ADLS directly, a thin film of fluorescein sodium salt solution (SIGMA, 46970-100G, Roedermark, Germany) coated on a coverslip with 50  $\mu\text{mol/L}$  concentration has been used. Its thickness is 2  $\mu\text{m}$ . By moving the calibration film vertically, the structure of the ADLS is visualized layer-by-layer using a SCMOS camera. From Figure 7b, it can be seen that the zeroth order light has been distantly moved from the modulated beams, showing negligible influence on the fluorescent measurement. The 3D distribution of ADLS was reconstructed using Matlab software, as shown in Figure 7c. The ADLS is 12  $\mu\text{m}$  wide, 12  $\mu\text{m}$  high, and  $d_s = 0.8 \mu\text{m}$  thick if a  $20\times$  NA 0.4 lens is applied. It is sufficiently large to cover the entire jet flow. The ADLS has a good uniformity. The standard deviation of the thickness is about 0.18  $\mu\text{m}$ .

#### 4. Results

The performance of the ADLSFC system is evaluated with the fluorescent micropillars and microspheres, respectively. Then, the mixture of the micropillars and microspheres is applied in the experiments to show the capability of distinguishing different samples in a wide size range.

##### 4.1. Detection of the Micropillars

First, the fluorescent micropillar with a relatively high concentration ( $\sim 10^7 \text{ mL}^{-1}$ ) is applied. A typical time trace of the fluorescence signal ( $I_f$ ) is plotted in Figure 8a for the measurement of fluorescent micropillars. It can be seen the raw fluorescent signal contains a large amount of noise, including optical noise, instrumental thermal noise, and electromagnetic noise. The presence of noisy signals can generate analysis errors on the FWHM of the pulse. Thus, a series of denoising methods have been applied to remove noise.

The result after processing is shown in Figure 8b. Here, a medium gain was applied to amplify the weak fluorescent signal. It can be seen that the peak fluorescence ( $I_{fp}$ ) of the micropillar signal is  $1.38 \times 10^4$  and  $\tau = 1.13 \text{ ms}$ . The diameter of the particle is 1.09  $\mu\text{m}$ , as estimated from Equation (3). With ADLSFC, micropillars with submicron sizes ( $d_p = 0.73 \mu\text{m}$  and  $d_p = 0.39 \mu\text{m}$ ) are also distinguished, as shown in Figure 8c–f.

Theoretically, the number of micropillars injected into the test chamber in 5 min is 833. Our measurement with the ADLSFC is 736, on average. The detection efficiency is  $\delta = 88.3\%$ . Since the theoretical particle number is estimated from the manufacturing value, the actual concentration of particles could be reduced according to many factors, e.g., sedimentation and adhesion. Thus, the injected number of particles must be smaller than the theoretical value. Accordingly, the actual  $\delta$  could be higher than 88.3%. The high detection efficiency reflects the high sensitivity of the system.



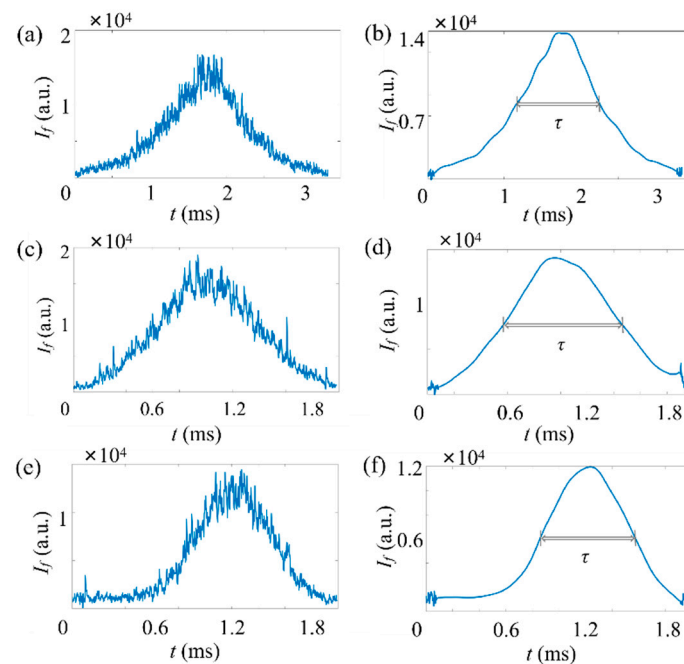


**Figure 8.** Typical time traces of fluorescence signals of micropillars in a low particle concentration,  $\sim 10^7 \text{ mL}^{-1}$ . Here,  $Q_s = Q_j = 1 \text{ } \mu\text{L/h}$ . The horizontal axis represents the time, and the vertical axis represents the signal strength. Here, a moderate gain is applied for the PMT. (a,c,e) Raw data and (b,d,f) data after noise reduction. (a,b) Time trace of micropillar with  $d_p = 1.09 \text{ } \mu\text{m}$ . (c,d) Time trace of micropillar with  $d_p = 0.73 \text{ } \mu\text{m}$ . (e,f) Time trace of micropillar with  $d_p = 0.39 \text{ } \mu\text{m}$ .

#### 4.2. Detection of the Microspheres

Then, the fluorescent microspheres are detected at a low concentration ( $\sim 8 \times 10^4 \text{ mL}^{-1}$ ), which commonly exists in biological and biomedical applications where large but sparse cells or bacteria targets are detected. A typical time trace of  $I_f$  is plotted in Figure 9a. The corresponding result after processing is shown in Figure 9b. Since the fluorescence of the  $5 \text{ } \mu\text{m}$  microsphere is relatively strong, a low gain was applied in the measurement. It can be seen that  $I_{fp}$  of the microsphere signal is  $3.68 \times 10^4$  and  $\tau = 3.46 \text{ ms}$ . The diameter of the particle is  $4.98 \text{ } \mu\text{m}$  from Equation (3). Theoretically, the number of microspheres injected into the test chamber in 5 min is 7. Our measurement with the ADLSFC is 7.3, on average. The detection efficiency is  $\delta = 104.3\%$ . The number of microspheres detected in the experiment is consistent with the theoretical one. The sensitivity of ADLSFC in detecting sparse targets is as expected.

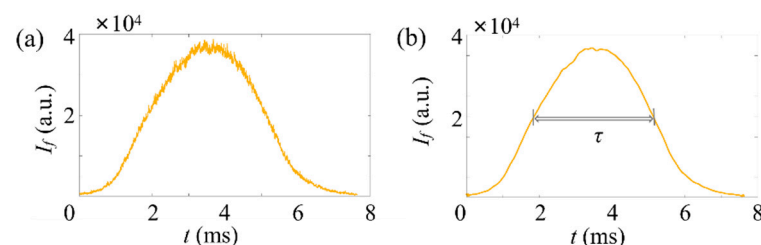


**Figure 9.** Typical time traces of fluorescence signals of microspheres in a low particle concentration,  $\sim 8 \times 10^4 \text{ mL}^{-1}$ . Here,  $Q_s = Q_j = 1 \text{ } \mu\text{L/h}$ . The horizontal axis represents the time, and the vertical axis represents the signal strength. Here, a low gain is applied for the PMT. (a) Raw data, (b) after noise reduction.

#### 4.3. Size Analysis of the Fluorescent Microspheres and Micropillars

Subsequently, to verify the accuracy of ADLSFC for sample size measurement, we analyzed the measured particle size. As shown in Figure 10, the blue bars indicate the

average diameters of micropillars and microspheres obtained by analyzing the FWHM of the fluorescence signals, and the yellow bars indicate the theoretical particle diameters. It can be seen the average  $d_p$  of the micropillar from the experiments is  $0.74\ \mu\text{m}$ , while that of the theoretical data is  $0.77\ \mu\text{m}$  (estimated from the diagonal size of the micropillars measured in SEM). The results measured using ADLSFC are highly consistent with that using SEM. Thus, the validity of ADLSFC to detect and measure the size of submicron scale particles has been supported. In addition, the  $d_p$  of the microsphere from the experiments is essentially consistent with the theoretical one. All these indicate that the ADLSFC can reliably evaluate the streamwise size of the particles at the moment of passing through the ADLS.

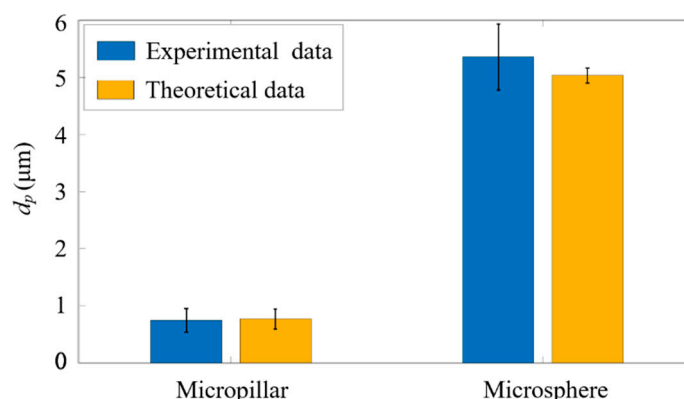


**Figure 10.** Experimental measurements versus theoretical particle size analysis. The blue histogram represents the size of the particles passing through ADLS. The theoretical data are estimated from SEM images of the particles.

It should be noted that when the flow rates of jet and sheath flows are both  $1\ \mu\text{L}/\text{h}$ , according to the variations of the flow rates, the particle velocity in the jet flow exhibits a 15% fluctuation around its mean value. According to Equation (3), the velocity fluctuations of the flow will lead to large fluctuations of particle diameter measurement if a large particle with large  $\tau$  passes through the ADLS. This is why in Figure 10, the measurement of the diameters of microspheres shows a large standard deviation at approximately  $0.58\ \mu\text{m}$ . The relative deviation is nearly 12%, which is larger than the nominal deviation value of 5%, and primarily attributed to the velocity fluctuations of particles.

#### 4.4. Detection of Mixed Microparticles with Different Proportions

Since the two fluorescent particles have significantly different sizes, the large fluorescent intensity difference may cause big difficulties in detecting the micropillars and microspheres simultaneously. In the detection of micropillars and microspheres separately above, two different gains have been applied. However, in the detection of mixed particle solution, we have to use a single gain. Therefore, in this section, we show whether ADLSFC can distinguish between the two particles from the mixed solution.

Before the experiment, the concentration of the particles and their ratio in the mixed solution is preliminarily determined through fluorescent image analysis, as shown in Figure 11. The micropillar solution is diluted 500 times, while the microsphere solution is diluted 60 times, and then mixed in equal volume. In theory, the particle density ratio ( $\beta = C_{pi}/C_s$ , where  $C_{pi}$  and  $C_s$  are the particle density of the micropillar and microsphere, respectively) between micropillars and microspheres is 15. The actual  $\beta$  obtained from the fluorescent image is approximately 16.67. The measurement result from the image method is approximately consistent with the theoretical one.

In this investigation, the micropillars and microspheres stock solutions were diluted 12,500 and 100 times, respectively. Theoretically, the diluted solution concentration was  $\sim 8 \times 10^5\ \text{mL}^{-1}$ . The two diluted solutions were mixed in the ratio of  $\beta = 1, 2$ , and 3, respectively.

First of all, we explored the capability of ADLSFC to measure particle size and distinguish different particles in the mixed solution. During the experiments, a medium gain was applied. The results are demonstrated by a two-dimensional probability density ( $P_d$ ) distribution in a two-parameter space, including the particle size  $d_p$  and the peak fluorescence intensity  $I_{fp}$ , as shown in Figure 12. Normally, the larger the particle size, the stronger the fluorescence. For instance, in Figure 12a, where  $\beta$  is 1, it can be clearly seen that  $P_d$  shows two different clusters in the parameter space. One is around  $d_p = 0.70 \mu\text{m}$  and the other is around  $d_p = 6.68 \mu\text{m}$ . The former is coincident with Figure 10, while the latter is slightly larger with occasional measurement extended to  $\sim 10 \mu\text{m}$ . This is because the medium gain leads to a saturation of fluorescent signal during analogue-to-digital conversion. Thus,  $I_{fp}$  is underestimated with the FWHM of the microspheres overestimated. Nevertheless, Figure 12a indicates that the micropillars and microspheres can be clearly distinguished by their sizes. Similar results are also observed in Figure 12b. In Figure 12c, due to the larger concentration of micropillars, the agglomeration of particles leads to separate spikes in the probability density distribution. Two clusters of particles with different sizes and peak intensities are still distinguishable. These results support the capability and reliability of measuring particle sizes and distinguishing the particles from their size information through ADLSFC.

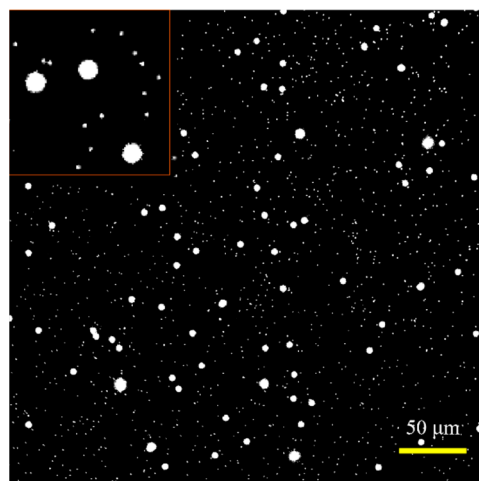


**Figure 11.** Fluorescence image of mixed micropillars and microspheres solution. The shape of the micropillar is not distinguishable from the image due to the low resolution. The red square in the upper left corner shows the zoom-in particle image.

The experimental observation of the ratios between micropillars and microspheres is compared with the theoretical ones, as shown in Figure 13. When the theoretical  $\beta$  is 1, 2, and 3, the experimental ones are 1.039, 2.252, and 3.394, respectively.

Although the experimental results for  $\beta$  are slightly higher than the theoretical ones, the average differences are within 10%. The small difference can be attributed to two reasons. One is that the particle density in the solution may fluctuate with time, resulting in a fluctuation of the theoretical particle density. The other is that the microspheres with larger size tend to precipitate at such a low flow rate. This leads to a higher ratio between the micropillars and microspheres. In general, the measured particle ratios are consistent with the actual ratios, and the system again exhibits sufficient accuracy in identifying and sorting fluorescent particles of different particle size.

The 2D  $P_d$  distribution provides not only the information on size distribution, but also intensity distribution information, which could imply the side area of the particle. Accordingly, two-dimensional information about an anisotropic sample, which might be important in biomedical and material investigations, can be revealed simultaneously.

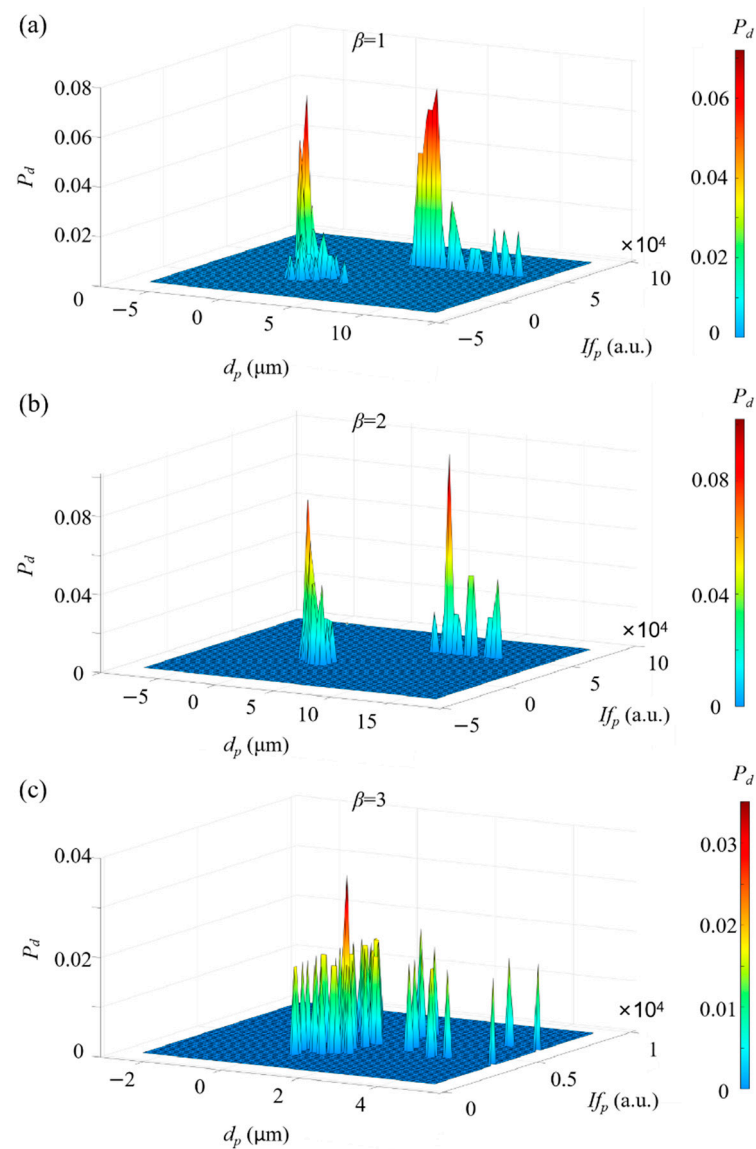


**Figure 12.** Two-dimensional probability density distribution of a mixed solution. (a)  $\beta = 1$ ; (b)  $\beta = 2$ ; (c)  $\beta = 3$ .

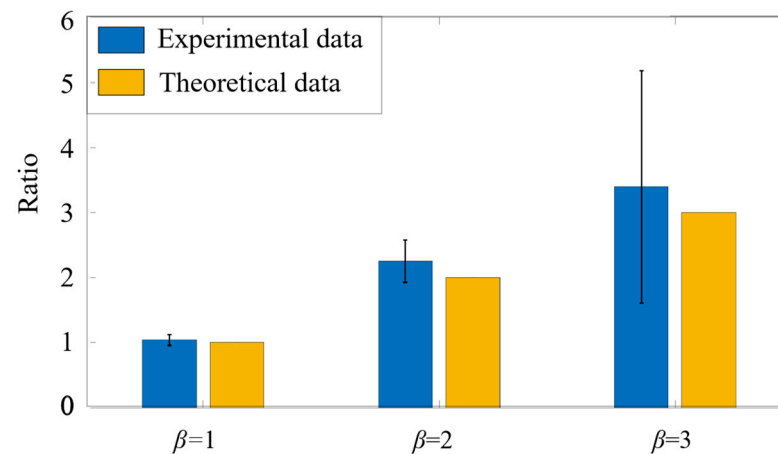


**Figure 13.** Comparison between the experimental ratios and the theoretical ones in the mixed solutions. The blue histogram represents the experimental measurement results, and the yellow histogram is used as a theoretical value comparison.

#### 4.5. Analysis of the Size Distribution of Fluorescent Micropillars

The micropillars have diverse sizes, with lengths of 0.4~1  $\mu\text{m}$  and widths of 0.3~0.6  $\mu\text{m}$ , while their attitudes when across the ADLS are unknown. Therefore, we analyzed the sizes of the micropillars when they pass through the ADLS to test the performance of ADLSFC in terms of distinguishing submicron size particles. The results are shown in Figure 14.

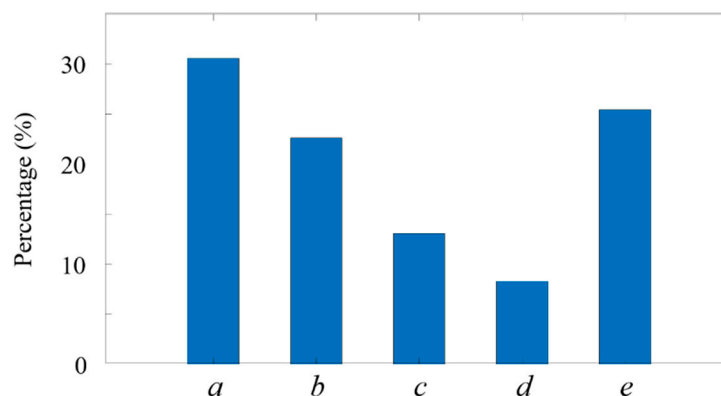


**Figure 14.** Percentage of fluorescent micropillars passing through ADLS. (a)  $0.2 \mu\text{m} \leq d_p \leq 0.4 \mu\text{m}$ , (b)  $0.4 \mu\text{m} < d_p \leq 0.6 \mu\text{m}$ , (c)  $0.6 \mu\text{m} < d_p \leq 0.8 \mu\text{m}$ , (d)  $0.8 \mu\text{m} < d_p \leq 1 \mu\text{m}$ , (e)  $d_p > 1 \mu\text{m}$ .

Among the measured micropillars, their sizes are highly non-uniform. In total, 30.6% of them are between 0.2 and 0.4  $\mu\text{m}$ , making up the highest portion (Figure 14, group a). In contrast, the micropillars between 0.8 and 1.0  $\mu\text{m}$  have the lowest portion (8.3%) in the solution (Figure 14, group b). Almost 25.4% of micropillars have a size over 1  $\mu\text{m}$ , and over half of the micropillars are below 0.4  $\mu\text{m}$ . The successful detection of the small micropillars, as shown in both Figures 10 and 14, indicates that the ADLSFC system is capable of capturing O (100 nm) particles, even using a 20 $\times$  lens. The sensitivity and resolution of the system can be further improved with a high magnification and numerical aperture lens. Furthermore, if samples with regular sizes are applied, the system can even reveal the attitudes of the samples through their sizes when they pass through the ADLS.

## 5. Discussion

In this investigation, the sampling rate of the system is 500 kHz, which provides the capability of achieving a high counting rate of samples. To test the counting rate in the current ADLSFC system, we set the flow rate of the jet and sheath flow to 20  $\mu\text{L}/\text{h}$  and detected the fluorescent micropillars with a concentration of  $2 \times 10^8 \text{ mL}^{-1}$ . Since the micropillars cannot pass through the ADLS regularly, to reveal the counting rate, the minimum time interval ( $\Delta\tau$ ) between two distinguishable micropillars from their fluorescent signals is investigated, as plotted in Figure 15. It can be seen that the minimum  $\Delta\tau$  is approximately 0.1 ms, which, in turn, indicates that the maximum count rate of our system is  $10^4$  events per second. It should be noted that when larger flow rates, smaller particles, or thinner light sheets are applied, the count rate can be even higher.

From the preliminary investigations above, the ADLSFC system has exhibited good accuracy and submicron resolution in terms of distinguishing different fluorescent samples from their sizes. The outstanding performance of the system provides us with a new approach for the detection and analysis of biological samples, e.g., *E. coli* (0.5~2  $\mu\text{m}$ ) [45], various blood cells (6~8  $\mu\text{m}$ ) [46], platelets (2~4  $\mu\text{m}$ ) [47], cell suspensions, and even extracellular vesicles (50~150  $\mu\text{m}$ ) in biological fluids [48,49]. Considering that a low magnification and NA objective lens have been used in this preliminary investigation, the performance of the ADLSFC system can be further improved to achieve much higher spatial resolution to distinguish different exosomes below 100 nm. Thereafter, whole blood analysis for disease diagnostic using ADLSFC could become practical.



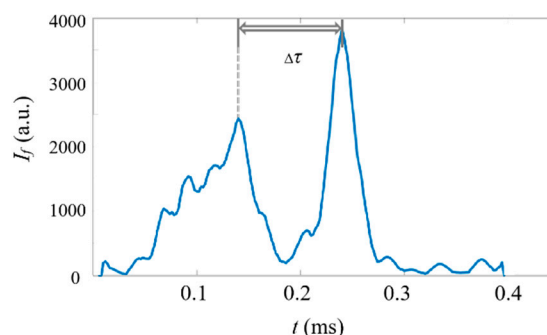


**Figure 15.** Typical time traces of fluorescence signals of micropillars in a concentration of  $2 \times 10^8 \text{ mL}^{-1}$ .  $Q_s = Q_j = 20 \text{ }\mu\text{L/h}$ . The horizontal axis represents the time and the vertical axis represents the signal intensity.  $\Delta\tau = 0.1 \text{ ms}$ .

## 6. Conclusions

In this research, we have developed a novel flow cytometry with an anti-diffraction light sheet. The light sheet is constituted of Bessel–Gaussian beams, which are parallelly and tightly aligned. With a large aspect ratio and small thickness, the ADLS can count and measure the sizes of particles and biological samples (e.g., cells) in a wide size range, from O (100 nm) to 10  $\mu\text{m}$ . Thus, screening the biological samples by their sizes can be easily achieved.

By using commercial fluorescent particles, including both micropillars and microspheres, the performance of the ADLS flow cytometry has been tested. The averaged particle detection efficiency is up to 96.3%. During the size analysis of particles in mixed solutions, the analytical error is within 10%. The analytical detection results match the theoretical values even at low particle density. All these fully demonstrate the good detection performance of ADLS flow cytometry, which could be an effective approach for micro/submicron-scale biological and particle material analysis and detection.

**Author Contributions:** Conceptualization, W.Z. and Y.Z.; methodology, W.Z., M.Z., T.Z. and Y.G.; software, Y.Z., T.Z. and M.Z.; validation, M.Z. and S.L.; formal analysis, M.Z. and Y.G.; investigation, Y.G., M.Z. and S.L.; resources, J.Y. and K.W.; data curation, S.L. and M.Z.; writing—original draft preparation, Y.G.; writing—review and editing, M.Z., Y.Z., W.Z., C.Z. and J.Y.; visualization, Y.G. and M.Z.; supervision, W.Z., C.Z., J.Y. and J.B.; project administration, J.B., K.W. and W.Z.; funding acquisition, W.Z., K.W. and J.B. All authors have read and agreed to the published version of the manuscript.

**Funding:** This investigation is supported by the National Natural Science Foundation of China (Grant No. 51927804, 61775181, 61378083).

**Data Availability Statement:** The data presented in this study are available on request from the corresponding author.

**Conflicts of Interest:** The authors declare that they have no known competing financial interest or personal relationships that could have appeared to influence the work reported in this paper.

## References

- McKinnon, K.M. Flow Cytometry: An Overview. *Curr. Protoc. Immunol.* **2018**, *120*, 5.1.1–5.1.11. [[CrossRef](#)] [[PubMed](#)]
- Barteneva, N.S.; Fasler-Kan, E.; Vorobjev, I.A. Imaging Flow Cytometry: Coping with Heterogeneity in Biological Systems. *J. Histochem. Cytochem.* **2012**, *60*, 723–733. [[CrossRef](#)] [[PubMed](#)]
- Elshal, M.F.; McCoy, J.P. Multiplex bead array assays: Performance evaluation and comparison of sensitivity to ELISA. *Methods* **2006**, *38*, 317–323. [[CrossRef](#)]
- Levine, L.S.; Hiam-Galvez, K.J.; Marquez, D.M.; Tennooren, I.; Madden, M.Z.; Contreras, D.C.; Dahunsi, D.O.; Irish, J.M.; Oluwole, O.O.; Rathmell, J.C.; et al. Single-cell analysis by mass cytometry reveals metabolic states of early-activated CD8<sup>+</sup> T cells during the primary immune response. *Immunity* **2021**, *54*, 829–844.e5. [[CrossRef](#)]
- Mei, H.E.; Leipold, M.D.; Maecker, H.T. Platinum-conjugated Antibodies for Application in Mass Cytometry. *Cytom. Part A* **2016**, *89*, 292–300. [[CrossRef](#)] [[PubMed](#)]

6. de Rutte, J.; Dimatteo, R.; Archang, M.M.; van Zee, M.; Koo, D.; Lee, S.; Sharrow, A.C.; Krohl, P.J.; Mellody, M.; Zhu, S.; et al. Suspendable Hydrogel Nanovials for Massively Parallel Single-Cell Functional Analysis and Sorting. *ACS Nano* **2022**, *16*, 7242–7257. [[CrossRef](#)] [[PubMed](#)]
7. Dittrich, P.S.; Tachikawa, K.; Manz, A. Micro total analysis systems. Latest advancements and trends. *Anal. Chem.* **2006**, *78*, 3887–3907. [[CrossRef](#)]
8. Erdem, K.; Ahmadi, V.E.; Kosar, A.; Kuddusi, L. Differential Sorting of Microparticles Using Spiral Microchannels with Elliptic Configurations. *Micromachines* **2020**, *11*, 412. [[CrossRef](#)]
9. He, M.; Crow, J.; Roth, M.; Zeng, Y.; Godwin, A.K. Integrated immunoisolation and protein analysis of circulating exosomes using microfluidic technology. *Lab Chip* **2014**, *14*, 3773–3780. [[CrossRef](#)]
10. Liascukiene, I.; Amselem, G.; Gunes, D.Z.; Baroud, C.N. Capture of colloidal particles by a moving microfluidic bubble. *Soft Matter* **2018**, *14*, 992–1000. [[CrossRef](#)]
11. Martel, J.M.; Toner, M. Particle Focusing in Curved Microfluidic Channels. *Sci. Rep.* **2013**, *3*, 340. [[CrossRef](#)]
12. Wang, Z.; Wu, H.-J.; Fine, D.; Schmulen, J.; Hu, Y.; Godin, B.; Zhang, J.X.J.; Liu, X. Ciliated micropillars for the microfluidic-based isolation of nanoscale lipid vesicles. *Lab Chip* **2013**, *13*, 2879–2882. [[CrossRef](#)] [[PubMed](#)]
13. Ward, M.D.; Kaduchak, G. Fundamentals of Acoustic Cytometry. *Curr. Protoc. Cytom.* **2018**, *84*, e36. [[CrossRef](#)] [[PubMed](#)]
14. Webster, C.; Pavlath, G.K.; Parks, D.R.; Walsh, F.S.; Blau, H.M. Isolation of human myoblasts with the fluorescence-activated cell sorter. *Exp. Cell Res.* **1988**, *174*, 252–265. [[CrossRef](#)] [[PubMed](#)]
15. Sosik, H.M.; Olson, R.J. Automated taxonomic classification of phytoplankton sampled with imaging-in-flow cytometry. *Limnol. Oceanogr. Methods* **2007**, *5*, 204–216. [[CrossRef](#)]
16. Mikami, H.; Kawaguchi, M.; Huang, C.J.; Matsumura, H.; Goda, K. Virtual-freezing fluorescence imaging flow cytometry. *Cold Spring Harb. Lab.* **2020**, *11*, 1162. [[CrossRef](#)] [[PubMed](#)]
17. Spitzer, M.H.; Nolan, G.P. Mass Cytometry: Single Cells, Many Features. *Cell* **2016**, *165*, 780–791. [[CrossRef](#)] [[PubMed](#)]
18. Scorzetti, G.; Brand, L.E.; Hitchcock, G.L.; Rein, K.S.; Sinigalliano, C.D.; Fell, J.W. Multiple simultaneous detection of Harmful Algal Blooms (HABs) through a high throughput bead array technology, with potential use in phytoplankton community analysis. *Harmful Algae* **2009**, *8*, 196–211. [[CrossRef](#)]
19. Han, Y.; Wang, S.; Zhang, Z.; Ma, X.; Li, W.; Zhang, X.; Deng, J.; Wei, H.; Li, Z.; Zhang, X.-E.; et al. In vivo imaging of protein-protein and RNA-protein interactions using novel far-red fluorescence complementation systems. *Nucleic Acids Res.* **2014**, *42*, e103. [[CrossRef](#)] [[PubMed](#)]
20. Leipold, M.D.; Newell, E.W.; Maecker, H.T. Multiparameter Phenotyping of Human PBMCs Using Mass Cytometry. *Methods Mol. Biol.* **2015**, *1343*, 81–95. [[CrossRef](#)]
21. Jiang, H.; Weng, X.; Li, D. Dual-wavelength fluorescent detection of particles on a novel microfluidic chip. *Lab Chip* **2013**, *13*, 843–850. [[CrossRef](#)] [[PubMed](#)]
22. Kanwar, S.S.; Dunlay, C.J.; Simeone, D.M.; Nagraath, S. Microfluidic device (ExoChip) for on-chip isolation, quantification and characterization of circulating exosomes. *Lab Chip* **2014**, *14*, 1891–1900. [[CrossRef](#)] [[PubMed](#)]
23. Lee, K.; Shao, H.; Weissleder, R.; Lee, H. Acoustic Purification of Extracellular Microvesicles. *Acs Nano* **2015**, *9*, 2321–2327. [[CrossRef](#)] [[PubMed](#)]
24. Wehrens, M.; Ershov, D.; Rozendaal, R.; Walker, N.; Schultz, D.; Kishony, R.; Levin, P.A.; Tans, S.J. Size Laws and Division Ring Dynamics in Filamentous *Escherichia coli* cells. *Curr. Biol.* **2018**, *28*, 972–979. [[CrossRef](#)]
25. Zhao, J.; You, Z. A Microflow Cytometer with a Rectangular Quasi-Flat-Top Laser Spot. *Sensors* **2016**, *16*, 1474. [[CrossRef](#)]
26. Taichi, M.; Hideharu, M.; Akihiro, I.; Takuro, I.; Yasuyuki, O.; Keisuke, G. On-chip light-sheet fluorescence imaging flow cytometry at a high flow speed of 1 m/s. *Biomed. Opt. Express* **2018**, *9*, 3424.
27. Zhu, Y.; Zhang, C.; Gong, Y.; Zhao, W.; Bai, J.; Wang, K. Realization of flexible and parallel laser direct writing by multifocal spot modulation. *Opt. Express* **2021**, *29*, 8698–8709. [[CrossRef](#)]
28. Khonina, S.N.; Kazanskiy, N.L.; Karpeev, S.V.; Butt, M.A. Bessel Beam: Significance and Applications—A Progressive Review. *Micromachines* **2020**, *11*, 997. [[CrossRef](#)]
29. Bouchal, P.; Kapitán, J.; Konečný, M.; Zbončák, M.; Bouchal, Z. Non-diffracting light in nature: Anomalously reflected self-healing Bessel beams from jewel scarabs. *APL Photonics* **2019**, *4*, 126102. [[CrossRef](#)]
30. Jiménez-Gambín, S.; Jiménez, N.; Benlloch, J.M.; Camarena, F. Generating Bessel beams with broad depth-of-field by using phase-only acoustic holograms. *Sci. Rep.* **2019**, *9*, 20104. [[CrossRef](#)]
31. Antonacci, G.; Domenico, G.D.; Silvestri, S.; Delre, E.; Ruocco, G. Diffraction-free light droplets for axially-resolved volume imaging. *Sci. Rep.* **2017**, *7*, 17. [[CrossRef](#)] [[PubMed](#)]
32. Du, Z.; Li, Y.; Chen, B.; Wang, L.; Hu, Y.; Wang, X.; Zhang, W.; Yang, X. Label-free detection and enumeration of rare circulating tumor cells by bright-field image cytometry and multi-frame image correlation analysis. *Lab Chip* **2022**, *22*, 3390–3401. [[CrossRef](#)]
33. Panwar, N.; Song, P.; Tjin, S.C.; Yong, K.T. Sheath-assisted hydrodynamic particle focusing in higher Reynolds number flows. *J. Micromechan. Microeng.* **2018**, *18*, 105018. [[CrossRef](#)]
34. Keller, P.J.; Schmidt, A.D.; Santella, A.; Khairy, K.; Bao, Z.; Wittbrodt, J.; Stelzer, E.H.K. Fast, high-contrast imaging of animal development with scanned light sheet-based structured-illumination microscopy. *Nat. Methods* **2010**, *7*, 637. [[CrossRef](#)]
35. Keller, P.J.; Schmidt, A.D.; Wittbrodt, J.; Stelzer, E. Reconstruction of Zebrafish Early Embryonic Development by Scanned Light Sheet Microscopy. *Science* **2008**, *322*, 1065–1069. [[CrossRef](#)]

36. Planchon, T.A.; Gao, L.; Milkie, D.E.; Davidson, M.W.; Galbraith, J.A.; Galbraith, C.G.; Betzig, E. Rapid three-dimensional isotropic imaging of living cells using Bessel beam plane illumination. *Nat. Methods* **2011**, *8*, 417. [[CrossRef](#)]
37. Fan, Y.-J.; Hsieh, H.-Y.; Tsai, S.-F.; Wu, C.-H.; Lee, C.-M.; Liu, Y.-T.; Lu, C.-H.; Chang, S.-W.; Chen, B.-C. Microfluidic channel integrated with a lattice lightsheet microscopic system for continuous cell imaging. *Lab Chip* **2021**, *21*, 344–354. [[CrossRef](#)] [[PubMed](#)]
38. Fan, Y.J.; Hsieh, H.Y.; Huang, Y.R.; Tsao, C.; Lee, C.M.; Tahara, H.; Wu, Y.C.; Sheen, H.J.; Chen, B.C. Development of a water refractive index-matched microneedle integrated into a light sheet microscopy system for continuous embryonic cell imaging. *Lab Chip* **2022**, *22*, 584–591. [[CrossRef](#)]
39. Girkin, J.M.; Carvalho, M.T. The light-sheet microscopy revolution. *J. Opt.* **2018**, *20*, 053002. [[CrossRef](#)]
40. Hedde, P.N.; Gratton, E. Selective plane illumination microscopy with a light sheet of uniform thickness formed by an electrically tunable lens. *Microsc. Res. Tech.* **2018**, *81*, 924–928. [[CrossRef](#)]
41. Heddleston, J.M.; Chew, T.L. Light sheet microscopes: Novel imaging toolbox for visualizing life's processes. *Int. J. Biochem. Cell Biol.* **2016**, *80*, 119–123. [[CrossRef](#)] [[PubMed](#)]
42. Voie, A.H.; Burns, D.H.; Spelman, F.A. Orthogonal-plane fluorescence optical sectioning: Three-dimensional imaging of macroscopic biological specimens. *J. Microsc.* **1993**, *170*, 229–236. [[CrossRef](#)] [[PubMed](#)]
43. Richards, B.; Wolf, E. Electromagnetic diffraction in optical systems, II. Structure of the image field in an aplanatic system. *Proc. R. Soc. A* **1959**, *253*, 358–379.
44. Leutenegger, M.; Rao, R.; Leitgeb, R.A.; Lasser, T. Fast focus field calculations. *Opt. Express* **2006**, *14*, 11277–11291. [[CrossRef](#)]
45. Looser, V.; Hammes, F.; Keller, M.; Berney, M.; Kovar, K.; Egli, T. Flow-cytometric detection of changes in the physiological state of *E. coli* expressing a heterologous membrane protein during carbon-limited fedbatch cultivation. *Biotechnol. Bioeng.* **2010**, *92*, 69–78. [[CrossRef](#)]
46. Grisendi, G.; Finetti, E.; Manganaro, D. Detection of microparticles from human red blood cells by multiparametric flow cytometry. *Blood Transfus.* **2015**, *13*, 274. [[PubMed](#)]
47. Stockelberg, D.; Hou, M.; Jacobsson, S.; Kutti, J.; Wadenvik, H. Detection of platelet antibodies in chronic idiopathic thrombocytopenic purpura (ITP). A comparative study using flow cytometry, a whole platelet ELISA, and an antigen capture ELISA. *Eur. J. Haematol.* **2009**, *56*, 72–77. [[CrossRef](#)]
48. Song, F.; Wang, C.; Wang, C.; Gao, J.; Han, L. Enrichment-Detection Integrated Exosome Profiling Biosensors Promising for Early Diagnosis of Cancer. *Anal. Chem.* **2021**, *93*, 9860–9868. [[CrossRef](#)] [[PubMed](#)]
49. Sturk, A.; Grootemaat, A.E.; Gardiner, C.; Nieuwland, R.; Harrison, P.; Sturk, A.; van Leeuwen, T.G.; Nieuwland, R. Particle size distribution of exosomes and microvesicles determined by transmission electron microscopy, flow cytometry, nanoparticle tracking analysis, and resistive pulse sensing. *Thromb. Haemost.* **2014**, *12*, 1182–1192.

**Disclaimer/Publisher's Note:** The statements, opinions and data contained in all publications are solely those of the individual author(s) and contributor(s) and not of MDPI and/or the editor(s). MDPI and/or the editor(s) disclaim responsibility for any injury to people or property resulting from any ideas, methods, instructions or products referred to in the content.